Influence of underlying interlevel dielectric films on extrusion formation in aluminum interconnects

Fen Chen,[a] Baozhen Li, Timothy D. Sullivan, Clara L. Gonzalez, Christopher D. Muzzy, H. K. Lee, and Mark D. Levy
IBM Microelectronics Division, 1000 River Street, Essex Junction, Vermont 05452

Michael W. Dashiell and James Kolodzey
Electrical and Computer Engineering, University of Delaware, Newark, Delaware 19716

(Received 25 February 2000; accepted 28 August 2000)

Knowledge of the mechanical properties of interlevel dielectric films and their impact on submicron interconnect reliability is becoming more and more important as critical dimensions in ultralarge scale integrated circuits are scaled down. For example, lateral aluminum (Al) extrusions into spaces between metal lines, which become more of a concern as the pitches shrink, appear to depend partially on properties of SiO_2 underlayers. In this article nanoindentation, wafer curvature, and infrared absorbance techniques have been used to study the mechanical properties of several common interlevel dielectric SiO_2 films such as undoped silica glass using a silane (SiH_4) precursor, undoped silica glass using a tetraethylorthosilicate precursor, phosphosilicate glass deposited by plasma-enhanced chemical vapor deposition and borophosphosilicate glass (BPSG) deposited by subatmosphere chemical vapor deposition. The elastic modulus E and hardness H of the as-deposited and densified SiO_2 layers are measured by nanoindentation. The coefficients of thermal expansion (CTE) of the densified layers are estimated by temperature-dependent wafer curvature measurements. Fourier transform infrared spectroscopy is used to obtain the chemical structures of all SiO_2 layers. Among the four common interlevel layers, BPSG exhibits the smallest modulus/hardness and a relatively small amount of moisture loss during anneal. The BPSG shows the highest CTE, which generates the smallest thermal stress due to a closer match in the CTE between Al and SiO_2. BPSG again has the lowest as-deposited compressive stress and the lowest local Si–O–Si strain before annealing. The center frequency of the Si–O bond stretching vibration exhibits a linear dependence on total film stress. The shifts of Si–O peaks for all the SiO_2 layers also correlate well with the stress hysteresis obtained from wafer curvature measurements. Stress interactions between the various SiO_2 underlayers and the Al metal film are also investigated. The impact of dielectric elastic properties on interconnect reliability during thermal cycles is proposed. © *2000 American Vacuum Society*. [S0734-211X(00)04206-2]

I. INTRODUCTION

SiO_2-based thin films, such as undoped, phosphorous doped and boron–phosphorous doped silicate glass are extensively exploited as interlevel dielectrics (ILDs) in the current multilevel metallization technologies.[1–3] These films are usually deposited at high temperatures so that mechanical stress is generated in both the ILD and metal layers due to the difference of thermal expansion coefficients and macroscopic Young's modulus between different layers and the Si substrate. When it arises in ULSI metallization and passivation systems, this stress can lead to metal line voiding, hillocks, extrusions, cracking, poor adhesion, delamination, and eventually complete mechanical failure of the circuit. Hillock and extrusion growth during annealing and thermal cycling of metal films are associated with the relaxation of compressive thermal stress in these films.[4] The continued scaling down to submicron device geometries has further increased susceptibility to stress related problems,[5] including hillock and extrusion formation. Metal line shorts have been caused by vertical aluminum (Al) hillocks between different metal levels and by lateral extrusions into spaces between metal lines at the same level, as the ILD thickness and pitches shrink to make larger and faster circuits.[6]

In addition to tighter geometries, mechanical and thermal properties of different ILDs can affect extrusion behavior. Wafers using identical metallization, but deposited on different underlying oxides, can exhibit dramatically different lateral metal extrusion behavior. We found that extrusions are infrequent after metal annealing for metallization deposited on doped silica glass, but are very common for metallization on undoped silica glass. In some cases, such extrusions are large enough to short neighboring lines after anneal. In other cases, although initial shorting is not observed, postpassivation leakage through the ILD occurs. The frequency and size of lateral Al extrusions therefore appear to be influenced by the underlying SiO_2 layers, making knowledge of the mechanical properties of these common ILDs films and their influences on aluminum copper (AlCu) interconnects of great interest.

Although a number of previous investigations have been devoted to vertical hillock suppression, no detailed study of lateral extrusion suppression has been performed to date.

[a]Electronic mail: chenfe@us.ibm.com

TABLE I. Characteristic parameters of the CVD silicate glass films analyzed. T is the deposition temperature and t is the film thickness.

Glass	Characteristics	Source	T (°C)	t (μm)
Silane	Silicate glass, undoped	SiH_4	400	0.5/2.0
TEOS	Silicate glass, undoped	TEOS	350	0.5/2.0
BPSG	B (4.5%) and P (4.2%) doped silicate glass	TEOS, TEPO, and TMB	440	0.5/2.0
PSG	P (4%) doped silicate glass	SiH_4 and PH_3	570–580	0.5/2.0

Rocke and Schneegans[7] reported that the use of TiN refractory overcoating layer on the metal lines reduced the hillock formation. This method is very effective for vertical hillocks but not for lateral extrusion. Learn[8] proposed decreasing the chemical vapor deposition (CVD) temperature of ILD films to control the hillock and extrusion growth. But reduction of deposition temperature may compromise ILD quality. Kim *et al.*[9] investigated the stress behavior of various phosphosilicate glass (PSG) films and observed a relation between the stress behavior of PSG film and hillocks on the metal film, but their study was limited to PSG films.

In the present work, results for studies on common ILD SiO_2 films are reported: undoped silica glass using a silane (SiH_4) precursor, undoped silica glass using a tetraethylorthosilicate (TEOS) precursor, PSG deposited by plasma-enhanced chemical vapor deposition (PECVD), and borophosphosilicate glass (BPSG) deposited by subatmosphere CVD. Elastic modulus E and hardness H of the different SiO_2 films were obtained by nanoindentation. Macroscopic temperature dependent mechanical stresses were obtained from wafer curvature measurements. Microscopic film strains were estimated from Fourier transform infrared spectroscopy (FTIR), and surface morphology of various ILD films was measured using atomic force microscopy (AFM). An in-line defect detection system was used to demonstrate the relation between lateral Al extrusions and the properties of various ILD SiO_2 films. The influence of ILD elastic properties, moisture absorption/desorption, and surface morphology on Al extrusion is shown, and the most suitable ILD material was identified for minimizing metal extrusions.

II. EXPERIMENTAL PROCEDURES AND ANALYSIS

Four different oxide films were deposited on three sets of 200-mm-diam (100)-Si substrates. The first set of wafers received films with a thickness of 0.50 μm, the second set of wafers received a thickness of 2.0 μm, and the third set of wafers was deposited with a 0.50 μm thick oxide film followed by a Ti/AlCu/Ti/TiN metal stack (10/342/13/32 nm). The deposition characteristics are summarized in Table I together with values of thickness, dopant concentration, and deposition technique. The first set of oxide films was used for stress and strain measurements. These wafers duplicated the oxide thickness of patterned wafers used for extrusion morphology and density analysis. The second, thicker set of films was used for hardness and stiffness measurements, and the third set was used for studies of stress interaction between underlying SiO_2 films and overlying Al metal stack.

The indentation test was performed on both as-deposited and annealed samples, using a Nanoidenter II (Nano Instruments, Oak Ridge, Tennessee). All the indentations were performed under a constant load rate mode whereby a Berkovitch indenter (three-sided pyramid) with a tip radius smaller than 100 nm was driven into the oxide films at a controlled load rate.[10] A hold segment was inserted at the end of each loading segment to allow time for the system to equilibrate before unloading. Then an unloading segment followed at a constant unloading rate. The theoretical resolution of displacement and load is about 0.04 nm and 75 nN, respectively. The early unloading portion was used for stiffness calculation, and the hold segment was used for thermal drift correction. The absolute uncertainty of the evaluated mechanical properties was judged to be on the order of 5% in most cases by using 2.0 μm instead of 0.5 μm thick films to minimize the substrate effects. As the rule of thumb,[11] only those data points with depth up to 10% of the ILD film thickness were used to calculate elastic constants. For each condition, about 20 identical indents were made to ensure the reproducibility and accuracy.

The unloading stiffness S is determined by linear fitting of the unloading data and the contact depth h_c, and a is calculated by

$$h_c = h_t - \varepsilon \frac{P}{S}, \tag{1}$$

where h_t is maximum depth of penetration including elastic deformation of the surface under load, P is the maximum load, and ε is a geometrical constant ($\varepsilon = 0.75$ for a parabola of rotation). The projected area A of actual contact can be expressed as a function of the form

$$A = a h_c^2 + b h_c + c h_c^{1/2} + d h_c^{1/4} + \cdots, \tag{2}$$

where a, b, c, d, ... are adjustable constants and are obtained from the diamond tip calibration. Once the area of contact A is determined, hardness is calculated using the corresponding load P:

$$H = \frac{P}{A}. \tag{3}$$

Finally, the elastic modulus is derived from stiffness data using Sneddon's solution[12]

$$S = \frac{dP}{dh} = \frac{2}{\sqrt{\pi}} E_r \sqrt{A}, \tag{4}$$

where S is the stiffness, P is the load, h is the displacement, A is the contact area, and E_r is the composite modulus for the indenter–sample combination. E_r is given by

$$E_r=\left[\frac{1-\nu^2}{E}+\frac{1-\nu_i^2}{E_i}\right]^{-1}, \tag{5}$$

where E and ν are Young's modulus and Poisson's ratio for the sample and E_i and ν_i are Young's modulus and Poisson's ratio for the indenter.

The ILD film stresses were measured using an optical levered laser beam apparatus furnished with a hot stage capable of temperature up to 900 °C (Tencor-KLA FLX-2908 thin film stress measurement). Wafer curvatures were measured with and without the films at various temperatures. Wafers with films were ramped to 600 °C and annealed for 30 min in nitrogen to simulate processing. The ramp rate was 20 °C/min and measurements were obtained every 10 °C. The stress in the film σ_f, was calculated using Stoney's formula[13]

$$\sigma_f=\frac{E_s}{1-\gamma_s}\frac{t_s^2}{6t_f}\left(\frac{1}{R_1}-\frac{1}{R_2}\right), \tag{6}$$

where E_s and γ_s are Young's modulus and Poisson's ratio for the substrate, t_s and t_f are the substrate and film thickness, and R_1 and R_2 are the radii of curvature before and after film deposition, respectively.

If the values of the elastic constants for both substrate and film are assumed to be constant in the temperature range considered, the temperature dependence of the stress can be described in this linear region by the following equation:[14]

$$\Delta\sigma_f=(\alpha_s-\alpha_f)\frac{E_f}{1-\gamma_f}\Delta T, \tag{7}$$

where α_s and α_f are the thermal expansion coefficients of substrate and film, and E_f and γ_f are Young's modulus and Poisson's ratio for the film, respectively.

Chemical and structural properties before and after anneal were examined by measuring the absorbance of different SiO_2 samples using FTIR spectroscopy. Optical absorption data were collected on a Nicolet 740 FTIR using a quartz beamsplitter and PbSe detector. Transmission through the thin film and the substrate was measured and the substrate absorption was removed by calibrating measured data against the substrate with the top SiO_2 removed by wet chemical etching. The most important vibration band in the SiO_2 films is the Si–O stretching vibration band at ~1050–1100 cm^{-1}. Measuring the center frequency ν of this band allows the determination of the strain using the relation

$$\varepsilon=\frac{\nu-\nu_0}{\nu_0}, \tag{8}$$

where ν_0 is the frequency for relaxed SiO_2 films. The microscopic model for strain and its relationship to the elastic properties of the SiO_2 films can be further investigated by using

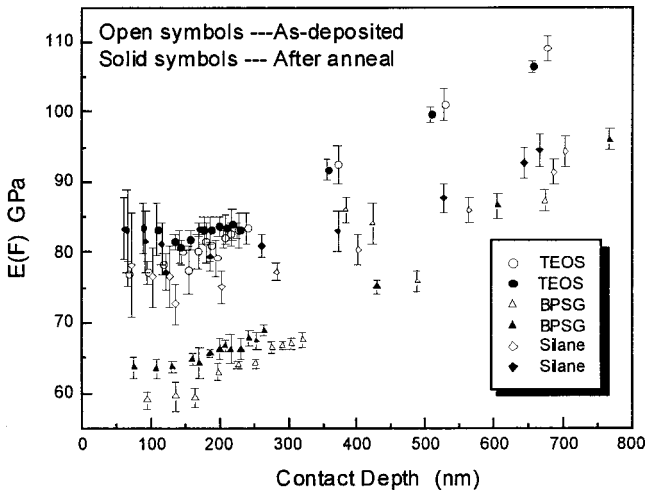

FIG. 1. Calculated modulus E vs contact depth for silane, TEOS, BPSG, and PSG as-deposited and annealed films from nanoindentation measurements. Among them, BPSG exhibits the smallest as-deposited and annealed E values.

$$\sigma=\frac{E_f}{1-\gamma_f}\varepsilon. \tag{9}$$

III. RESULTS

A. Elastic properties

Figures 1 and 2 show calculated E and H data versus contact depth for silane, TEOS, PSG, and BPSG oxide films. Doped silicate glasses show smaller E and H than undoped silicate glasses and BPSG has the smallest E and H values. The modulus values were nearly constant at a depth shallower than 200 nm and started to increase with indenter depth after 200 nm for silane and TEOS. This increase of E with indenter depth after about 10% film thickness is due to Si substrate effect. The hardness value of BPSG is only about 40%–50% of the silane and TEOS. Annealing caused

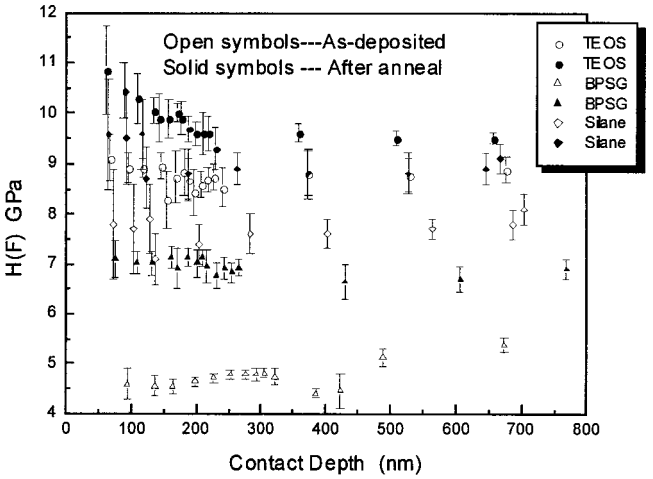

FIG. 2. Calculated hardness H vs contact depth for silane, TEOS, BPSG, and PSG as-deposited and annealed films from nanoindentation measurements. Among them, BPSG exhibits the smallest as-deposited and annealed H values, but the anneal effect on BPSG is most significant.

TABLE II. Elastic properties of various CVD silicate glass films. The $E/(1-\nu)$ results of this work are compared with a number of other results taken from references.

Oxides	H (GPa) (bef/aft ann.)	E (GPa) (bef/aft ann.)	Poisson ratio ν	$E/(1-\nu)$ (GPa) (bef/aft ann.)
This work				
Silane	7.6/9.0	75/79	0.25[a]	100/105
TEOS	8.7/9.8	80/82	0.25[a]	107/109
BPSG	4.5/7.0	59/64	0.17[b]	71/77
PSG	NA/NA	NA/NA	0.3[a]	NA/NA
Published data				
Silane				80[a]
				100[c]
TEOS				85[a]
				77[d]
BPSG				
(4% P, 3% B)				60[e]
(4% P, 3% B)				40[e]
(6% P, 2% B)				71[b]
PSG				
(3% P)				74[a]
(4% P)				70[e]
(4% P)				90[e]

[a]Reference 28.
[b]Reference 29.
[c]Reference 23.
[d]Reference 30.
[e]Reference 31.

about 50% hardness increase of BPSG but only 10%–20% of silane and TEOS. The average E and H values from the data in the contact depth range of 90–200 nm are listed in Table II for both as-deposited and annealed samples together with some published data for comparison. Among the four common ILDs studied here, BPSG exhibited the smallest modulus.

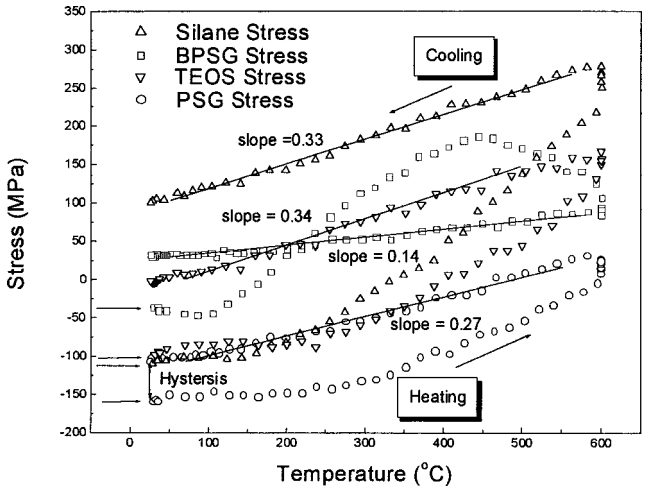

FIG. 3. Stress as a function of temperature for silane, TEOS, BPSG, and PSG oxide films during thermal cycling. Arrows indicate initial (as-deposited) stresses.

TABLE III. Intrinsic stress, stress hysteresis, and CTE of various CVD silicate glass films. The CTE results of this work are compared with a number of other results taken from references.

Oxides	Intrinsic stress (MPa)	Stress hysteresis (MPa)	CTE aft annealing ($10^{-6}\,°C^{-1}$)
This work			
Silane	−110	195	1.57
TEOS	−98	94	1.36
BPSG	−37	68	2.78
PSG	−160	56	NA
Published data			
Silane			1.37[a]
			2.67[b]
TEOS			1[c]
			2.61[b]
BPSG			0.51[a]
PSG			1.45[b]
			0.15[a]

[a]Reference 29.
[b]Reference 28.
[c]Reference 30.

B. Thermal stress

As shown in Fig. 3, the initial as-deposited stresses are different, indicating different intrinsic stresses in those films. These intrinsic stresses can be modulated by the deposition conditions such as temperature,[15] chamber pressure,[15] gas flow rate,[16] plasma power and frequency,[17] etc., as well as the material composition. Among four ILD films studied here, BPSG exhibited the smallest intrinsic compressive stress (37 MPa) and PSG exhibited the highest intrinsic compressive stress (160 MPa). During the first heating cycle, stress became progressively more tensile with increasing temperature. During the 30 min anneal at 600 °C, the tensile stress continued to increase suggesting densification. During cooling after densification, the stress–temperature curves were straight with a slope that can be accounted for by thermal expansion effects. Stress hysteresis (the difference between the film stress as-deposited and at the end of a complete thermal cycle) occurred in all oxide films after first annealing, suggesting that changes occurred in the composition or structure of the film.[18] Further cycling or ramping produced reversible linear stress–temperature changes with the same slopes as the first cooling curves and no stress hysteresis. Following Eq. (7), temperature-dependent stress measurements allow independent estimation of the thermal expansion coefficient of SiO_2 films when using elastic constants obtained from nanoindentation. Measured stress hysteresis and calculated coefficients of thermal expansion (CTE) values for the four oxide films are shown in Table III, along with values from other investigations. As seen in the published data, a spread in CTE for the same oxide was found even within the same research group, perhaps because of different process conditions. Nevertheless, some of our results are in good agreement with published results for PECVD deposited SiO_2. Strictly speaking, our reported CTE

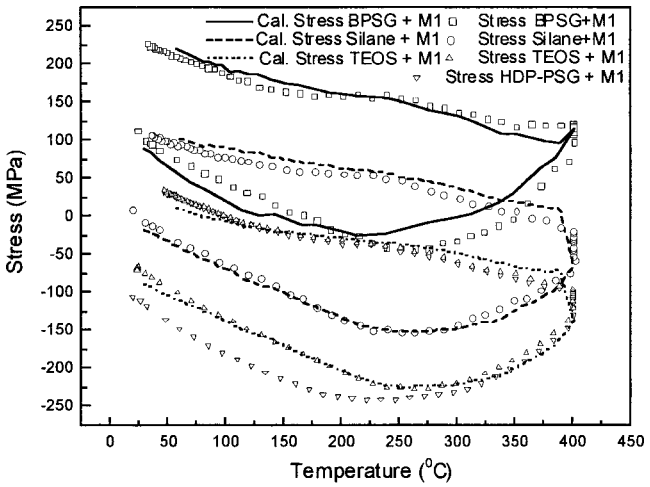

FIG. 4. Stress vs temperature for metal+various oxide composite films. The dash lines are the calculated stress curves by using Eq. (10).

values are only valid for annealed oxide films. Of the four films we studied, BPSG yielded the highest CTE.

Thermal stress interaction between SiO_2 and AlCu metal stack was also investigated by wafer curvature measurements. Figure 4 illustrates the temperature dependence of stress for the various composite SiO_2+AlCu layers on heating and on cooling. The same metal stack was deposited on four different underlying oxides. In addition, a single AlCu metal stack layer was also deposited on Si substrate as a reference sample. Comparisons of various SiO_2+AlCu composite films to single AlCu stack film show that shapes of all composite film (in particular the stress hysteresis) were dominated by the contribution of the AlCu metal stack. The dashed curves are the calculated stress curves using the relationship

$$\sigma_{\text{total}} t_{\text{total}} = A(\sigma_{\text{oxide}} t_{\text{oxide}} + \sigma_{\text{metal}} t_{\text{metal}}) + B. \quad (10)$$

The calculated values for σ_{total} are in reasonable agreement with the measured ones suggesting that plastic flow and deformation characteristics the of AlCu metal stack were not significantly affected by the presence of SiO_2 films. However, the absolute compressive stress of each composite film indeed was affected by underlying SiO_2.

C. Chemical and structural properties

Figure 5 shows the FTIR absorbance spectra for BPSG and silane SiO_2 films before and after anneal. The most significant features in these spectra are labeled in the figure. The features include the Si–O rocking band at ~450 cm^{-1}, the Si–O bending band at ~810 cm^{-1}, the Si–O stretching band at ~1070 cm^{-1}, the P–O band at ~1310 cm^{-1}, B–O band at ~1360 cm^{-1}, the B–O–B band at ~680 cm^{-1}, and the Si–O–B band at ~900 cm^{-1}. Si–O stretching bands shifted to a higher wave number and the bands were narrowed for all SiO_2 films after anneal, as also shown in Fig. 5.

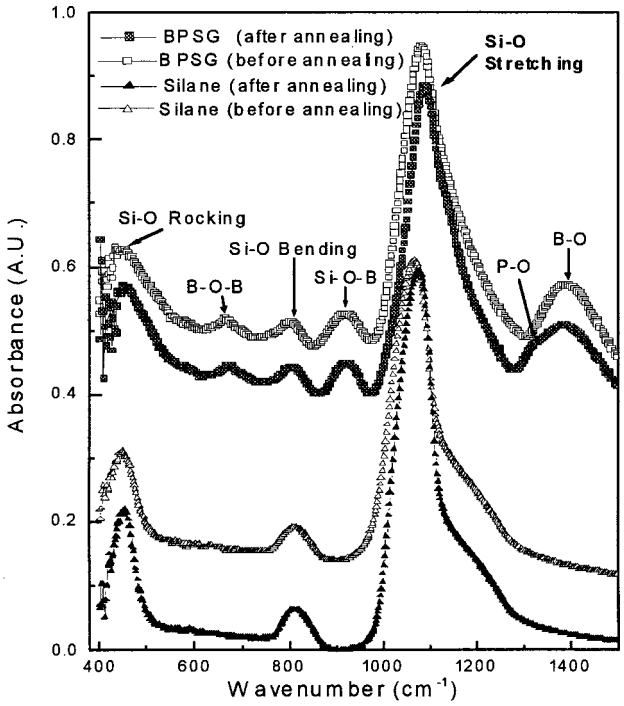

FIG. 5. FTIR absorbance spectra for silane and BPSG oxide films before and after anneal. The most significant features are labeled in the figure.

D. Surface roughness

Initial studies indicated that elastic properties of underlying oxide films could influence extrusion growth. However, other factors such as oxide surface roughness and surface energy related to surface bond configuration, could also affect extrusion formation and growth. Substrate surface roughness has been found to influence the overlying film crystallographic orientation for Ti and Ti/AlCu films deposited on various oxides.[19] Decrease of the surface roughness leads to an improved crystallographic texture in Ti, AlCu, Ti/AlCu, and Ti/TiN/AlCu films. The effects of various AlCu deposition temperatures and Ti-based underlayers on the resultant texture in AlCu tended to be secondary in nature. Good texture corresponds to a uniformly well-oriented metal film, which restricts grain boundaries to those formed due to difference in rotational orientation between grains. These boundaries presumably permit less atomic flux. Hence, if extrusion growth is dominated by boundary diffusion, oxide surface roughness can be important, and it is necessary to check the surface roughness values of various SiO_2 films and to further confirm the best candidate for extrusion control. Surface roughness was measured by AFM after oxide deposition, after metal deposition, and after metal annealing, respectively. Table IV shows the roughness results for all the oxide films with different conditions. The as-deposited BPSG and TEOS films have relatively smoother surface indicating that they should yield better Ti/AlCu texture. The following as-deposited metal surface roughness and annealed metal surface roughness were significantly en-

TABLE IV. Measured surface roughness for as-deposited oxide.

Oxides	As-deposited oxide surface roughness (nm)
Silane	3.1
TEOS	1.1
BPSG	1.15
PSG	1.4

hanced, which was partially due to the oxide surface energy difference and the metal stress relaxation difference during anneal.

IV. DISCUSSION

Stress interactions between SiO_2-based glass ILD and an AlCu metal stack can be qualitatively described by a rigid wall model as shown in Fig. 6. The force exerted by either metal or glass could be expressed as follows:

$$F=\sigma A=E\varepsilon A, \tag{11}$$

where A is the metal–glass contact area, σ is the stress, E is the modulus, and ε is the strain. During anneal, forces exerted by glass and metal should be balanced:

$$\begin{aligned} &F_G=F_M, \\ &E_G\varepsilon_G=E_M\varepsilon_M, \\ &\varepsilon_M=\varepsilon_G(E_G/E_M), \end{aligned} \tag{12}$$

where subscript G and M refer to glass and metal, respectively. From Eq. (12) we clearly see that metal can expand more to relax its built-in stress if oxide has a lower modulus. The uniform expansion of metal minimizes the localized extrusions during thermal ramping and anneal. Another important parameter to control extrusion is a biaxial compressive stress generated from changes in temperature as described by Eq. (7). This stress is the driving force for the growth of extrusions. The thermal mismatch stress is determined by the value of coefficients of thermal expansion α_{SiO_2} relative to that of the metal film. There is an appreciable mismatch between SiO_2 and AlCu; $\alpha_{SiO_2} \ll \alpha_{AlCu}$ so that the stress in the metal becomes more compressive as the films are heated. In order to reduce the compressive stress at the glass and metal interface, we have to choose the glass with the highest CTE and smallest modulus. The smaller the difference between the CTE of glass and metal, the smaller the thermal stress produced in metal film. Therefore, it is desirable to use glass with low modulus and high CTE to control the formation and growth of AlCu extrusions. In addition to the modulus and CTE, other factors such as glass surface roughness, intrinsic stress of the glass, moisture desorption from glass during anneal, and glass surface energy could also affect the microstructure of the AlCu overlayer[17,20,21] and the growth of AlCu extrusions.

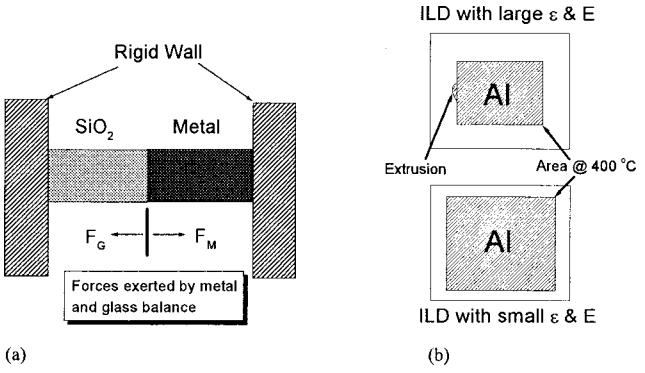

FIG. 6. (a) Rigid wall model for the force interaction between SiO_2 and metal. Forces exerted by glass and metal are balanced. (b) Al metal film thermal expansion during anneal with different ILD glass films. Al metal can stretch out more to relax its built-in compressive stress if ILD has lower modulus. The uniform stretch out of metal film minimizes the localized extrusion nucleation.

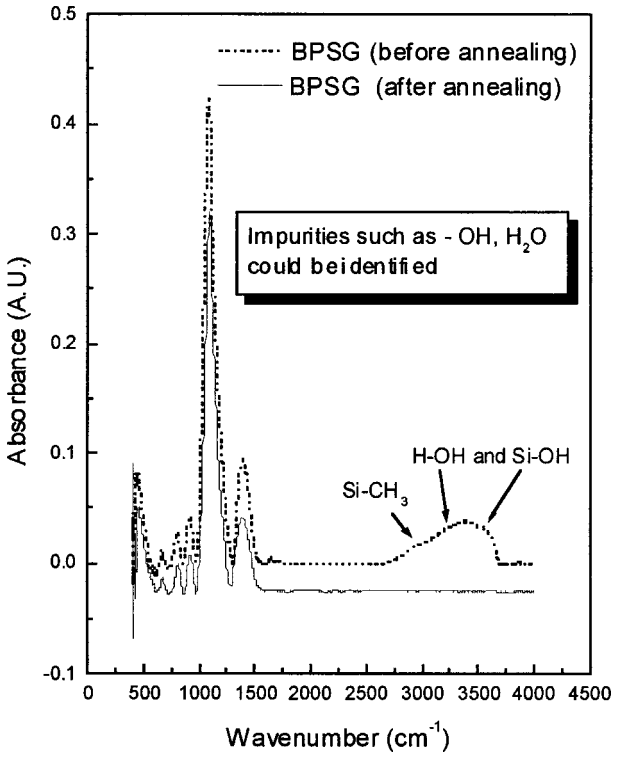

FIG. 7. FTIR absorbance spectra of a BPSG film as-deposited (dotted line) and after an anneal up to 600 °C (solid line). A disappearance of the absorption due to H–OH, Si–CH_3, and Si–OH groups can be obtained.

Nanoindentation results indicated that boron is more effective in reducing E and H than phosphorus because of its lower valence and smaller atom size. The modulus and hardness reduction improves when mixing B and P dopants. Based on the rigid wall model, the smaller the modulus, the better the extrusion control. Therefore, BPSG offers the best elastic properties among the four common ILDs studied here. Infrared (IR) absorption spectra for as-deposited and annealed films were illustrated in Fig. 7, showing that the typical absorptions due to hydrogen-bonded Si–OH groups and absorbed water disappear after a 600 °C 30 min anneal. Therefore, we concluded that the major effect caused by anneal is moisture desorption. Water is a byproduct of the deposition reaction and some is trapped during deposition. More moisture could be absorbed at room temperature dur-

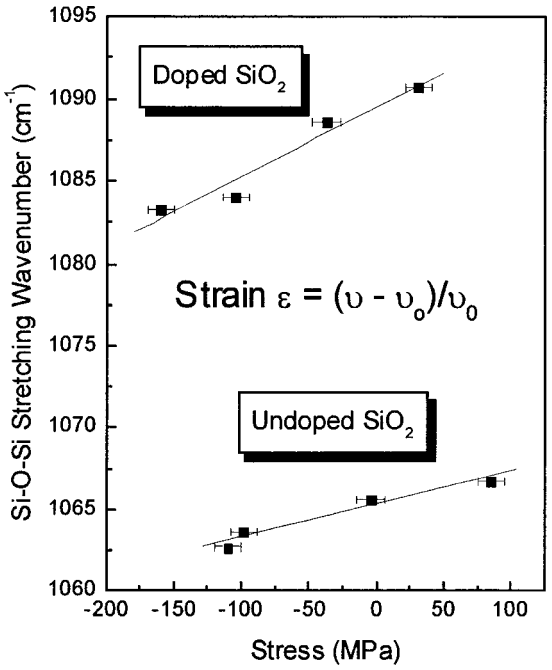

FIG. 8. Wave numbers of Si–O stretching band vs the mechanical stresses in various oxide films. The wave number values obey a linear function of the stress values.

ing storage. Annealing causes both an E and H increase for all the films but the impact on BPSG is the most significant, suggesting that the doped films become more sensitive to moisture as the total concentration of dopants increases. It is interesting to note that the hardness values for silane and TEOS annealed films decreased with indenter depth initially, then saturated at about 250 nm. Due to the softness of BPSG, its modulus started to increase earlier at about 150 nm depth. Since the moisture effect on hardness is clearly identified, we attributed this initial hardness decrease to the surface moisture desorption effect. The film surface probably desorbed more moisture than the bulk did during anneal. Therefore, the top of the film became harder than the bulk portion.

Stress–temperature curves showed a nonlinear stress change from compressive to highly tensile, which was attributed to a loss of water on heating. Heating can densify the films and build up tensile stress.[22] IR absorbance measurements confirmed a loss of water during anneal. The typical absorptions due to hydrogen-bonded Si–OH groups and absorbed water [(3300–3600) cm^{-1}] disappeared after 600 °C annealing for all the films. A reduction of tensile stress at around 400 °C was observed only for BPSG. It can be explained by the reflow due to weaker Si–O bonds in BPSG.

We further experimentally proved that the stress hysteresis was mainly due to the structure state changes caused by a loss of water. A later storage of these annealed samples in a temperature and humidity chamber (temperature=85 °C and relative humidity=85%) for 20 h did influence the water content and brought back the stress hysteresis. van Schravendijk *et al.* reported a similar influence of moisture absorption on stress hysteresis.[17] Due to the adverse effects of moisture in the films, stress hysteresis may be a good monitor for the amount of water loss during anneal. A high temperature annealing for silane oxide before metal deposition appears to minimize the adverse effects of moisture in the oxide films and decrease extrusion shorting. From the stress hysteresis values in Table III, we concluded that BPSG yielded moderate water loss.

TABLE V. Calculated elastic constants from strain–stress relationship of various PECVD silicate glass films. The modulus results from this calculation are two times smaller than the modulus results from nanoindentation.

Oxides	Strain (10^{-3}) bef/aft annealing	Stress (MPa) bef/aft annealing	$E/(1-\nu)$ (MPa) bef/aft annealing strain+stress	$E/(1-\nu)$ (MPa) bef/aft annealing nanoindentation
Silane	−2.5/1.3	−110/85	44/65	100/105
TEOS	−1.7/0.2	−98/−4	58/[a]	107/109
BPSG	−0.8/1.0	−37/31	46/31	71/77
PSG	−5.7/−5	−160/−104	28/21	NA/NA

[a]No meaningful result could be obtained due to different signs (−: compressive, +: tensile) of strain and stress.

For the oxide+metal composite films, increasing temperature provided a linear decrease of the stress level following an elastic regime as shown in Fig. 4. At about 220–275 °C (elastic–plastic transition temperature), plastic deformation and stress relaxation occurred leading to stress reduction. A fairly rapid drop in stress was observed only at about 400 °C, which was due to the $TiAl_3$ layer formation by chemical reaction between Ti and AlCu. The observed stress curves suggest that the critical period for extrusion formation is during metal anneal ramping and most of the growth takes place even before reaching the anneal target temperature, 400 °C. Usually, the smaller the compressive stress and the higher the elastic–plastic transition temperature, the better it is for extrusion control since both the driving force and thermal diffusion time were limited. Again the BPSG+AlCu system showed the smallest compressive and the highest transition temperature among four oxide+metal systems. The highest compressive stress for BPSG+AlCu was about 43 MPa occurring at 275 °C.

The very intense absorbtion band of Si–O stretching vibration of FTIR spectra is often used for strain analysis.[23,24] P–O and B–O bands are often found to contain the most information concerning the phosphorus and boron concentration in the films.[25] The band upshift and narrowing can be explained by an increase in bond strain due to densification during annealing.[26] Incorporation of impurities (P and B) into SiO_2 shifted the Si–O stretching bands to a higher wave number as expected.[26] The center frequencies of the Si–O stretching bands were estimated by careful peak fit. We found that Voigt-type peak-shape functions can give a good fit with a confidence factor close to 1. Figure 8 shows that this frequency varies with the stress of the SiO_2 films. Obviously, the values for the as-deposited as well as the annealed samples obey a linear function, which is expected considering Eqs. (8) and (9). The center frequencies of doped and undoped samples followed the different linear dependence of stresses. It is interesting to note that the films of zero stress have a center frequency near 1065 cm^{-1} for undoped samples and 1089 cm^{-1} for the doped samples, respectively,

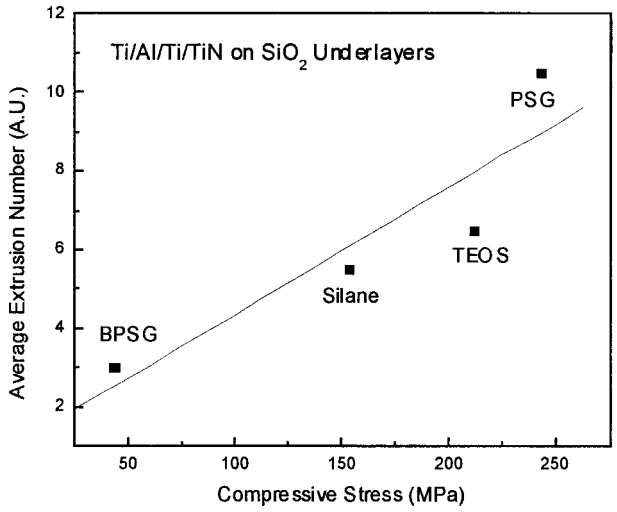

FIG. 9. Extrusion study after 400 °C 20 min anneal for AlCu metal stack on silane, TEOS, BPSG, and PSG underlying oxide films. Extrusion density tracks with the compressive stress of the composite films. BPSG underlying sample exhibits the smallest number of extrusion defects as consistent with previous elastic property results.

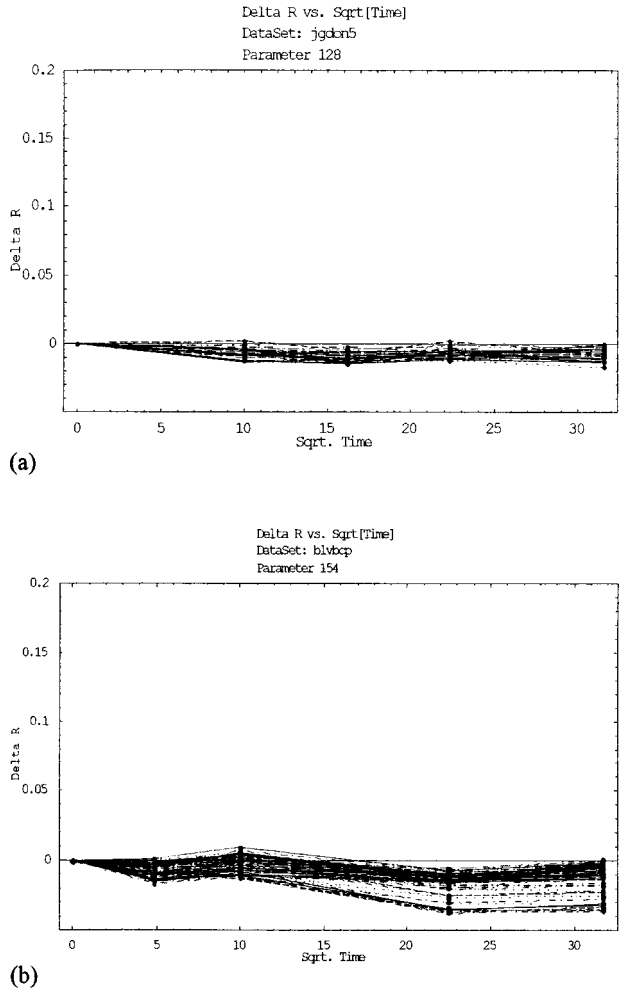

FIG. 10. (a) 225 °C 1000 h stress migration result of 0.35 μm $\times$ 400 000 μm Ti/AlCu/Ti/TiN metal serpentine structure with BPSG ILD; (b) 225 °C 1000 h stress migration result of 0.35 μm $\times$ 400 000 μm Ti/AlCu/Ti/TiN metal serpentine structure with silane ILD. No significant difference between BPSG and silane was observed for stress voiding.

corresponding to the values for relaxed oxides.

The microscopic strain and the elastic constants could be calculated from Eqs. (8) and (9). The results are shown in Table V. The elastic modulus values were different significantly (2×) from the one we estimated from the nanoindentation measurements. Incidentally, Ambrée *et al.* and Fitch *et al.* obtained similar discrepancies in the determination of the elastic constant of thermally grown and PECVD grown SiO_2 films.[23,27] The dynamic behaviors of other molecular bands such as Si–Si, Si–H, and Si–OH are not taken into account during strain measurement by IR spectroscopy, which focuses more on the local structure of the Si–O stretching bonds. The discrepancy between the local Si–O–Si strain and the total macroscopic film stress measurements originate from the fact that the macroscopic film stress depends not only on the mechanical behavior of the Si–O bonds but also on that of other bonds.[23] Therefore, special care must be taken when using physical quantities of different origin and order of magnitude to deduce the elastic constants. Furthermore, it may be that only a portion of Si–O bonds play a role in the local strain configurations, and further enhance the elastic constant differences. As shown in Table IV, BPSG showed the relatively small local strain before and after anneal, which again is beneficial to the extrusion control.

Based on mechanical and structural properties of various underlying SiO_2 films, BPSG was found to have lower elastic modulus, lower local strain, higher thermal expansion coefficient, and smoother surface than the other three oxides tested (silane, TEOS, and PSG), thus this oxide would be expected to help in relieving metal compressive stress and minimizing extrusion defects better than the other three. In order to evaluate the extrusion behavior of the different SiO_2 layers, a set of patterned wafers was fabricated. An in-line defect counting system and scanning electron microscopy were used to check the extrusion density and morphology. The extrusion defect counting results are shown in Fig. 9. Extrusion density tracks with the compressive stress of the composite films. The BPSG underlying film exhibited the smallest density of extrusion defects during anneal. Stress migration and electromigration tests were also performed on patterned wafers with BPSG and silane ILD oxides, respectively. Figure 10 shows the stress migration at 225 °C up to 1000 h for a total of 92 AlCu 0.35 μm $\times$ 400 000 μm serpentine structures encapsulated by BPSG and silane, respectively. No significant difference between the metal stack with BPSG ILD and the metal stack with silane ILD was observed for stress voiding. Electromigration results showed similar results. Therefore, we propose that extrusion may be more sensitive to the elastic difference of underlying oxide than stress migration voiding and electromigration voiding.

Finally, we want to emphasize that the present article only concentrated on underlying ILD effects on AlCu metal ex-

trusion control. Several other factors likely to affect extrusion growth, not reported here, include metallurgy changes to minimize mass transport path and nucleation sites and improve texture, process changes to reduce stress, and oxide chemical-mechanical polish (CMP) changes to reduce surface roughness.

V. CONCLUSIONS

In summary, the mechanical properties of common PECVD grown interlevel dielectric films used in electronic devices and their influences on Al interconnect reliability were investigated by various methods. Knowledge of these properties in PECVD grown silicate glass films is important to control thermally induced extrusion defects. Our mechanical property studies suggest that among four silicate glass films, BPSG has the lower elastic modulus, lower strain, a higher expansion coefficient, and smoother surface than the other oxides examined and minimizes extrusions with Al metallurgy. Expectations based on our basic mechanical property measurements were confirmed by extrusion experiments on patterned wafers. It should be noted that while BPSG has attractive mechanical properties, the choice of ILD in silicon technology is also dictated by other factors, with dielectric constant and the associated capacitances being perhaps the most important.

ACKNOWLEDGMENTS

The authors gratefully acknowledge John Aitken, Carl Carney, and Jennifer Lynch for helpful discussions and process support. The authors also wish to express their thanks to Jack Hay for his helpful suggestion regarding nanoindentation measurements.

[1]S. Nguyen, D. Dobuzinsky, D. Harmon, R. Gleason, and S. Fridman, J. Electrochem. Soc. **137**, 2209 (1990).
[2]S. Rojas, L. Zanotti, A. Borghesi, A. Sassella, and G. V. Pignatel, J. Vac. Sci. Technol. B **11**, 2081 (1993).
[3]Y. S. Obeng, K. G. Steiner, A. N. Velaga, and C-S. Pai, AT&T Tech. J. **73**, 94 (1994).
[4]S. P. Murarka, *Metallization: Theory and Practice for VLSI and ULSI* (Butterworth-Heinemann, Boston, 1993), p. 231.
[5]P. A. Flinn, D. S. Gardner, and W. D. Niz, IEEE Trans. Electron Devices **ED34**, 689 (1987).
[6]G. C. Schwartz, K. V. Srikrishnan, and A. Bross, *Handbook of Semiconductor Interconnection Technology* (Marcel Dekker, New York, 1998), p. 223.
[7]M. Rocke and M. Schneegans, J. Vac. Sci. Technol. B **6**, 1113 (1998).
[8]A. J. Learn, J. Vac. Sci. Technol. B **4**, 774 (1986).
[9]E. Kim, S.-H. Kang, and S.-K. Lim, Mater. Res. Soc. Symp. Proc. **356**, 495 (1995).
[10]Nano IndenterII Operating Instructions, Version 2.2 (Nano Instruments, Inc., Knoxville, TN, 1996).
[11]W. C. Oliver and G. M. Pharr, J. Mater. Res. **7**, 1564 (1992).
[12]J. W. Harding and I. N. Sneddon, Proc. Phys. Soc. London **78**, 169 (1961).
[13]G. G. Stoney, Proc. R. Soc. London, Ser. A **82**, 172 (1909).
[14]B. Bhushan, S. P. Murarka, and T. Gerlach, J. Vac. Sci. Technol. B **8**, 1068 (1990).
[15]H. Gokan, A. Morimoto, and M. Murahata, Thin Solid Films **149**, 85 (1987).
[16]J. Batey and E. Tierney, J. Appl. Phys. **60**, 3136 (1986).
[17]B. van Schravendijk, A. S. Harrus, G. Delgado, B. Sparks, and C. Roberts, Proceedings VMIC, 1992, p. 372.
[18]K. Ramkumar, S. K. Goshh, and A. N. Saxena, J. Electrochem. Soc. **140**, 2669 (1993).
[19]K. P. Rodbell, V. Svilan, L. M. Gignac, P. W. Dehaven, R. J. Murphy, and T. J. Licata, Mater. Res. Soc. Symp. Proc. **428**, 261 (1996).
[20]H. Honda, K. Touchi, and K. Hashimoto, Jpn. J. Appl. Phys., Part 1 **34**, 1037 (1995).
[21]A. S. Harrus, B. van Schravendijk, J. Park, and E. van de ven, Proceedings of the Electrochemical Society 1991, Ext. Abstr. 228, PV91-2, p. 322.
[22]P. A. Flinn, Mater. Res. Soc. Symp. Proc. **138**, 41 (1988).
[23]P. Ambrée, F. Kreller, R. Wolf, and K. Wandel, J. Vac. Sci. Technol. B **11**, 614 (1993).
[24]T. M. Niemczyk, L. Zhang, D. M. Haaland, and K. J. Radigan, J. Vac. Sci. Technol. A **16**, 3490 (1998).
[25]J. E. Franke, L. Zhang, T. M. Niemczyk, D. M. Haaland, and K. J. Radigan, J. Vac. Sci. Technol. A **13**, 1959 (1995).
[26]W. A. Pliskin and H. S. Lehman, J. Electrochem. Soc. **112**, 1013 (1965).
[27]J. T. Fitch, G. Lucousky, E. Kobeda, and E. A. Irene, J. Vac. Sci. Technol. B **7**, 153 (1989).
[28]G. Carlotti, L. Doucet, and M. Dupeux, J. Vac. Sci. Technol. B **14**, 3460 (1996).
[29]L. Doucet and G. Carlotti, Mater. Res. Soc. Symp. Proc. **356**, 215 (1995).
[30]J-H. Zhao, T. Ryan, P. S. Ho, A. J. Mckerrow, and W-Y. Shih, J. Appl. Phys. **85**, 6421 (1999).
[31]H. Bouchard, A. Azelmad, J. F. Currie, M. Munier, S. Blain, and T. Darwell, Mater. Res. Soc. Symp. Proc. **308**, 63 (1993).